Dynamical Bragg diffraction from crystalline colloidal arrays

Paul A. Rundquist, Panos Photinos, Seshadri Jagannathan, and Sanford A. Asher[a)]
Department of Chemistry, University of Pittsburgh, Pittsburgh, Pennsylvania 15260

(Received 2 February 1989; accepted 12 July 1989)

Polystyrene spheres with attached functional groups that ionize in solution repel one another; at sufficiently high sphere concentrations the spheres self-assemble into a crystalline lattice with lattice constants large enough to diffract visible light. We have experimentally and theoretically examined diffraction phenomena from colloidal crystals of polystyrene spheres of diameters between 69 and 127 nm in water. We relate the diffraction bandwidths to the sphere scattering powers in the context of the dynamical diffraction theory and demonstrate the importance of the dynamical theory for predicting the observed diffraction angles, intensities, and bandwidths. We also discuss the mechanism contributing to the diffuse scattering and show the significance of the coherent scattering by lattice phonons.

INTRODUCTION

Suspensions of colloidal particles show at relatively low particle concentrations, of the order of 1% by weight, a variety of phases with orientational[1,2] (e.g., tobacco mosaic virus) and/or translational[3–6] order (e.g., latex particles). Although these systems have been known for some time, they continue to be the subject of significant theoretical and experimental interest.[7–14] These systems mimic at the macroscopic level crystalline, liquid, and gas phases, and display phase transitions similar to those occurring in atomic and molecular systems.

The present work focuses on aqueous suspensions of monodisperse polystyrene spheres which spontaneously self-assemble into a variety of crystal structures. These crystal structures, as described here, depend upon the ratio of the sphere diameter to the nearest-neighbor sphere spacing, and also upon the solution ionic strength and the crystal boundary conditions. The polystyrene spheres self-assemble[15,16] due to repulsive interactions which derive from net charges on each sphere arising from ionization of surface sulfate groups which are attached during the sphere synthesis by the free radical emulsion polymerization.[17–19] At low ionic strengths the intersphere repulsive interactions can be significant over distances as long as 1 μm. To minimize these repulsive interactions, the spheres in the suspension adopt a regular arrangement on a crystalline lattice. The lattice constant of the resulting colloidal crystal can be of the order of several sphere diameters, i.e., comparable to the wavelength of visible light. The lattice constant is often clearly manifested by the brilliant iridescent colors exhibited by colloidal crystals. The iridescence is the result of Bragg diffraction of visible light by the crystal facets of the sample.[4,20,21] The Bragg diffraction of light by colloidal crystals is analogous to the diffraction of x rays by atomic and molecular crystals. An important difference, however, is the fact that the lattice constants of the colloidal crystals can be varied over a substantial range. Thus the Bragg diffraction by colloidal crystals can be tuned to cover the near-UV, the visible, and the near-IR spectral regions.

The unique diffraction properties of colloidal crystals, and single crystals in particular, have important applications, for example, as narrow-band rejection filters in areas of optics and spectroscopy. Recently, we demonstrated[22,23] the utility of a collodial crystalline filter to selectively and efficiently reject the Rayleigh scattering in a high-sensitivity simple Raman spectrometer.

It is important to characterize the diffraction properties of colloidal crystals, and to develop theoretical models which predict the diffraction phenomena. Recently, Spry and Kosan[24] applied x-ray dynamical diffraction theory for a rigid-lattice, nonabsorbing crystal to describe the transmittance and Bragg diffraction of light in these crystals, and presented relations which predict the wavelength dependence of the half-width of the diffraction peak and the transmittance of colloidal crystals as a function of the crystal structure and the refractive index mismatch between the spheres and the surrounding medium. They demonstrated that the colloidal crystals have sufficiently high diffraction efficiencies so that a crystal of polystrene spheres 50 layers thick diffracts essentially all incident light that satisfies the Bragg condition.

Here we present results of a systematic study of five large colloidal crystals which were prepared using spheres with diameters in the range between 69 and 127 nm. We examined the intensity of the transmitted, Bragg diffracted, and diffusely scattered light as a function of wavelength, angle of incidence, and sphere size. We also examined the dependence of the crystal structure and of the angular and wavelength bandwidths of the Bragg diffracted light as a function of the sphere size. Our results show that for light satisfying the Bragg condition the transmitted intensity is indeed negligibly small, but the measured maximum Bragg diffracted intensity is much lower than that expected for a rigid lattice. Furthermore, the diffusely scattered intensity is large, and increases with sphere size, and shows anomalous behavior about the Bragg angle. We show that the use of dynamical diffraction theory in the thick crystal limit is nec-

[a)] To whom correspondence should be addressed.

 0021-9606/89/204932-10$02.10

essary for the interpretation of the experimental data, and that the deviations from the simple Kinematic theory are significant. Indeed the observed diffraction angles deviate considerably from expectations based simply on Bragg's law. From the experimental results we determine the structure factor for the unit cell and compare the results to the scattering factor predicted by the Rayleigh–Gans theory. In addition, we discuss mechanisms contributing to the diffuse scattering, and show the significance of the coherent scattering by lattice photons.

EXPERIMENTAL

Monodisperse polystyrene spheres were prepared using synthetic procedures which will be described in detail elsewhere.[25] All sphere sample were dialyzed and treated with Bio-Rad AG 501-X8 mixed-bed ion exchange resin. The ion exchange resin was cleaned using a technique similar to that of Vanderhoff and Van den Hul.[26–28] The colloid sphere diameters were determined using transmission electron microscopy (TEM) by comparing sample micrographs to micrographs of standard latex particles. The standard deviations in size were determined by measuring 50–100 spheres The sphere diameters were also measured by quasi-elastic light scattering (QELS). The results of the two methods agreed to within $\pm$ 2 nm. The sphere diameters are listed in Table I, along with the total number of titrated charge groups per sphere for each sphere sample, as determined from conductometric titrations.[27] The 82 nm diameter polystrene spheres were purchased from Duke Scientific Corporation (batch 7202). These spheres were manufactured by Dow Diagnostics with a reported diameter of 91 nm with a polydispersity standard deviation of 6.4%, but our TEM and QELS measurements for these spheres both show diameters of 82 nm with a polydispersity standard deviation of 9%.

The different sphere size samples were filtered through cotton, which was boiled and soaked in water with ion exchange resin. The samples were then diluted with ultrapure water until each gave a transmission minimum for normal incidence in a quartz flow cell at approximately $\lambda = 500$ nm in order to maintain similar interplanar layer spacings. Unless otherwise specified, the wavelengths are those measured in air. The wavelength at the transmission minimum for normal incidence, λ_{90}, and the interplanar spacing, d, for each sample are also listed in Table I. The transmission spectra of the colloid samples were obtained using an IBM model 9420 UV-visible absorption spectrophotometer. Five crystal samples were constructed, using the different diameter spheres, according to previously reported procedures.[29] The colloid crystal thicknesses were approximately 0.4 mm.

Figure 1 illustrates the experimental geometry employed to measure the diffracted, transmitted, and diffusely scattered intensities as a function of the angle of incidence. The 488 nm line of a Spectra Physics model 164 argon-ion laser was incident on the crystal which was mounted on a calibrated rotation stage. The accuracy of the angular measurements is estimated to be $\pm$ 0.5°. The intensities of the incident, transmitted, and diffracted light were measured with a Coherent model 210 laser power meter. The diffusely scattered light was measured with an EG&G FND-100Q photodiode. The diffusely scattered light intensity was measured at an angle of approximately 45° from the incident light propagation direction. A $\lambda/2$ plate was used to select the incident polarization, either parallel (π) or perpendicular (σ) to the incidence plane.

The spatial intensity profiles of the Bragg diffracted peak were measured with a 1 mm diameter optical fiber which was translated across the diffraction spot in a direction perpendicular to the incidence plane. A condensing lens collimated the light transmitted through the fiber. The light intensity was attenuated by a number of neutral density filters and a second lens focused the transmitted light onto a ground glass screen covering a Hamamatsu G-1115 GaAsP photodiode. The signal from the photodiode was recorded as a function of the position of the optical fiber. In addition, the transmission spectrum was measured for each crystal using an IBM 9420 absorption spctrophotometer.

The crystal structures were determined from the Kossel ring patterns. The crystals were immersed in rectangular glass tank filled with water. The Kossel ring patterns were traced on translucent sheets of paper using techniques similar to those previously reported.[30]

An Abbe refractometer was used to determine the refractive indices of ordered collodial sphere suspensions at $\lambda = 589.3$ nm. We require accurate values of the refractive index of the sample at 488 nm to correct for refraction and for the quantitative dynamical diffraction calculations. The refractive indices at $\lambda = 488$ nm, listed in Table I, were obtained using the Cauchy relations[31]:

TABLE I. Parameters for colloidal crystals. Sphere diameters, D; number of charge groups, Q; refractive index, n_s at 488 nm, wavelengths of transmittance minimum for normal incidence, λ_{90}; layer spacing, d; and the crystal structure. d refers to the (110) planes for the bcc crystals, and to the (111) planes for the fcc crystals.

D (nm)	Q	n_s	Lattice	λ_{90} (nm)	d (nm)
69 ± 8	1280 ± 190	1.3401	bcc	493.3	184.1
76 ± 6	1270 ± 190	1.3421	bcc	496.2	184.9
82 ± 7	3000 ± 450	1.3443	bcc	501.3	186.5
105 ± 11	2560 ± 380	1.3573	fcc	510.0	187.9
127 ± 9	2280 ± 340	1.3607	fcc	496.0	182.3

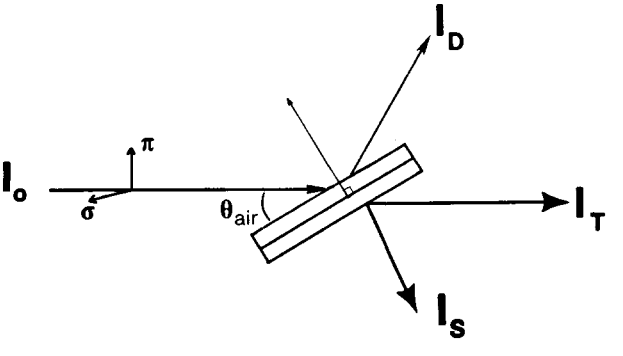

FIG. 1. Schematic of the experimental geometry.

$$n_w = 1.324 + 3046/\lambda^2, \quad (1)$$

$$n_p = 1.5683 + 10\,087/\lambda^2, \quad (2)$$

for λ in nm, and the relation[5]

$$n_s = n_w(1-\phi) + n_p\phi. \quad (3)$$

n_w, n_p, and n_s are the refractive indices of water, polystrene, and of the sample, respectively. ϕ is the volume fraction of polystyrene in the sample.

RESULTS

Figure 2 shows the observed Kossel ring patterns[30,32–34] for the colloidal crystals oriented such that the plane quartz windows enclosing the crystals lie parallel to the viewing plane. Kossel lines are produced by divergent sources of radiation within a crystal. Light diffusely scattered from the polystyrene spheres within the crystal and propagating at angles which do not satisfy the Bragg condition gives a diffuse illumination of the viewing plane. However, light propagating at angles that meet the Bragg condition cannot propagate through the crystal, and result in dark patterns on the viewing plane. Thus, the Kossel patterns map the transmission minima, resulting from the inability of the rays satisfying the Bragg condition to transmit out of the crystal. For a given wavelength, each set of reflecting planes produces a cone surface of minimum transmission. The axis of each cone is normal to the set of planes. Projection of these cones onto a planar screen results in a dark circle (if the set of reflecting planes is parallel to the screen) or ellipses (if the planes are at some other angle with respect to the screen).

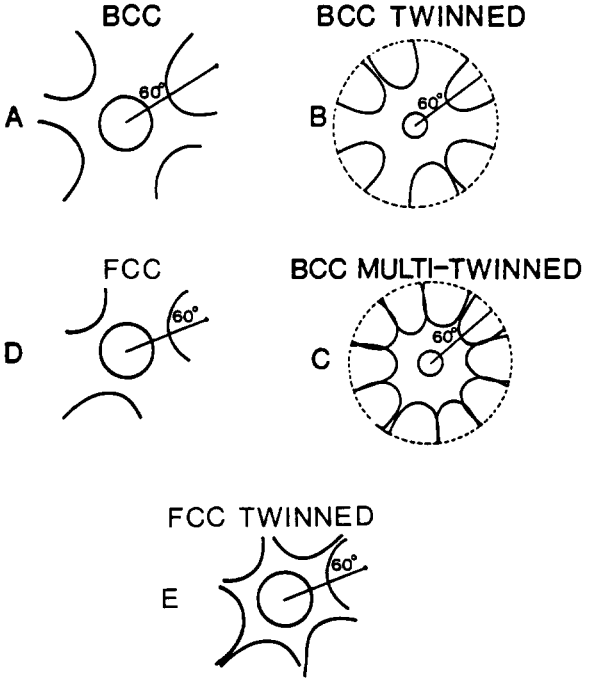

FIG. 2. Observed Kossel Ring patterns: (a) bcc single crystals; (b) bcc twinned; (c) bcc multitwinned; (d) fcc single crystal; (e) fcc twinned crystal. The 60° angles indicate the angles formed by the axes of the diffraction cones (the normals to the sets of planes).

Figure 2(a) shows the simple pattern exhibited by the 69 nm diameter sphere crystal which consists of a central ring surrounded by four ellipses. The central circle indicates that a set of planes is oriented parallel to the quartz surfaces. The axes of the four exterior Kossel rings occur at angles of 60° to the central ring and the angular widths of all of the rings are identical, indicating identical interplanar spacings. This pattern can only result from a body-centered-cubic (bcc) crystal structure where one (110) set of planes lies parallel to the quartz plates. The normals to the four other sets of (110) planes lie at 60° to that of the first set, and the corresponding rings appear as ellipses when projected onto the plane of the screen. The ellipses are separated by angles of 70.5° and 109.5°. These observations are in agreement with the results of Clark, Hurd, and Ackerson.[32]

The Kossel pattern was not altered by translating the colloidal crystal across the laser beam over an area of ~ 9 cm^2. We conclude that the 69 nm sample is a bcc crystal and that the orientation of the crystal axes is constant throughout the entire central portion of the sample, i.e., a single-crystal region of ~ 9 cm^2. However, for light incident at the edges of the sample the pattern becomes more complex. We can observe patterns as shown in Fig. 2(b) with two additional rings which result from twinning along a (110) plane. As illustrated in Fig. 3, the twin lattices are related by a 70.5° rotation about the (110) axis, to share one periodicity. Thus the twinning contributes only two new rings to the Kossel ring pattern. Because the laser beam spans both sides of the twin, both crystallites contribute to the Kossel ring pattern, and six rings simultaneously appear.[32,33] An even more complex Kossel pattern consisting of ten rings is shown in Fig. 2(c), and derives from multitwinned regions occasionally observed at the sample edges. The axes of the corresponding cones form 60° angles with the axis of the central Kossel ring.

Figure 2(d) shows a trigonal pattern from a face-centered-cubic (fcc) lattice where all four rings are derived from the fcc (111) planes. The wavelength of light used was too long to observe the fcc (002) planes in this case.

Figure 2(e) shows the hexagonally symmetric Kossel ring pattern commonly observed from the 105 nm sphere

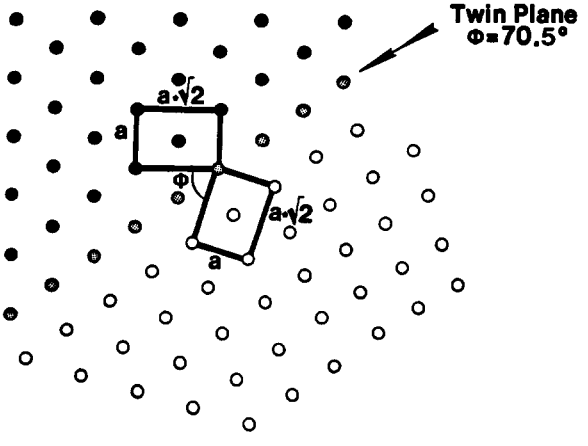

FIG. 3. Observed crystals twinning orientation for the bcc crystals.

diameter crystal in which a central ring is symmetrically surrounded by six ellipses of identical size. We observe a similar pattern for the 127 nm sphere diameter crystal. Although the symmetry suggests a hexagonal-close-packed (hcp) crystal structure, careful measurement of the Kossel pattern indicates that the rings are derived from a lattice spacing that is too large to be from the hcp (011) planes. Numerous studies have demonstrated the existence of a face-centered-cubic (fcc) structure at high sphere number densities.[30,32–34] At 488 nm incidence the Kossel pattern for a single fcc crystal should consist of a central ring surrounded symmetrically by three ellipses of identical size. The appearance of the three additional symmetrically displaced rings must be the result of crystal twinning. In contrast to the twinning observed for the 69 nm sphere diameter crystal, where lateral translation of the incident beam isolates one or the other crystallite, the six outer ellipse patterns observed for the 105 and 127 nm sphere diameter crystals persist as the laser beam is scanned across the quartz face, indicating that the twin plane or planes lie parallel to the quartz plates. The twins are related by a 60° rotation about the central (111) axis. We were unable to determine whether this twin derives from only one stacking fault or whether it derives from a number of stacking faults in the sample. We also examined the possibility that the crystal contained some hexagonal-close-packed stacked layers. We searched for additional Kossel rings associated with the (011) HCP layers. We were unable to clearly identify likely Kossel-ring candidates.

The colloidal crystal structure depends upon the sphere diameter, the sphere number density, and sphere charge, the ionic strength, the solution dielectric constant, and the sample temperature. Phase transitions as well as crystal melting can be achieved by appropriately varying these parameters.[20,35–38] For example, the sphere diameter increase from 82 nm to 105 nm induces a structural change from a bcc to an fcc lattice.

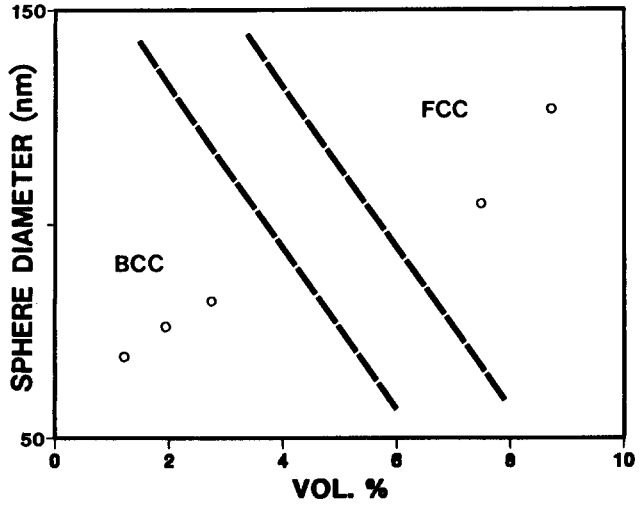

FIG. 4. Phases observed for the colloidal crystals as a function of sphere diameter and volume fraction. The distance between nearest-neighbor spheres is constant.

As seen in Table I, all of our samples were prepared with equal spacing of the planes responsible for the diffraction. Thus, the distance between nearest-neighbor spheres is the same for all the crystals. The sphere number density is constant within each crystal structure; however, the average number density increases by about 9% between the bcc and fcc lattice. Furthermore, the number of charges per sphere are reasonably similar and do not systematically differ for the 105 and 127 nm spheres compared to the smaller spheres. Thus, the actual sphere diameter increase appears to directly translate into a significant "effective sphere diameter" increase and results in the transition to the close-packed fcc lattice. As illustrated in Fig. 4, this significant increase in effective sphere diameter occurs in spite of the fact that the actual sphere diameter increase is relatively modest compared to the nearest-neighbor spacing of ~ 230 nm (which is greater than twice the 105 nm sphere diameter). This strong dependence upon actual sphere diameter was previously predicted in theoretical studies which proposed a strong dependence of the intersphere repulsive interactions on the actual sphere diameter.[39,40]

Figure 5 shows the measured diffracted and transmitted intensities, and the relative intensities of the diffuse scattering for the samples as a function of the angle θ_{xtl} for σ and π polarizations. The angle θ_{xtl} is derived from θ_{air} (see Fig. 1) using Snell's law. The diffracted and transmitted intensities were corrected for reflection losses and normalized to the incident beam intensity. The transmission bandwidths are broader than the diffraction bandwidths, and both bandwidths increase with increasing sphere diameter.

Figure 6 shows a three-dimensional plot of the dependence of diffracted intensity for the various sphere diameter crystals upon angle and the wavelength for the σ polarization incident light. The wavelength scale was simply calculated from Bragg's law, $\lambda = 2n_s d \sin\theta_{xtl}$, where λ is the wavelength in air, and d is the interplanar spacing (however, see below). The plot illustrates the dramatic increase in bandwidth with increasing sphere diameter. Although the transmitted intensity is essentially zero at the diffraction maximum, the relative (to the incident) intensity of the Bragg peak, D, is clearly less than unity in all cases. This difference mainly derives from diffuse scattering, since the absorption of polystyrene is negligible at the wavelengths used. The intensity of diffuse scattering, S, is shown in the lower panels of Fig. 5 as a function of the angle θ_{xtl}. The diffuse scattering intensities are proportional to the difference between the diffracted and transmitted intensities for each crystal. Anomalous peaks in the diffuse scattered intensity are observed at angles disposed about the diffraction angle. This phenomenon is most easily seen for the smaller diameter spheres. In all cases an asymmetry is present for S, where the diffusely scattered intensity is larger on the side closer to normal incidence.

Figure 7 shows the spatial intensity distribution about the Bragg peak for two different regions of the 69 nm diameter sphere sample. Diffraction from the central region of the crystal, which is well ordered, is shown by the triangles while the circular data points derive from the edge where defects are more likely. For this measurement we carefully chose

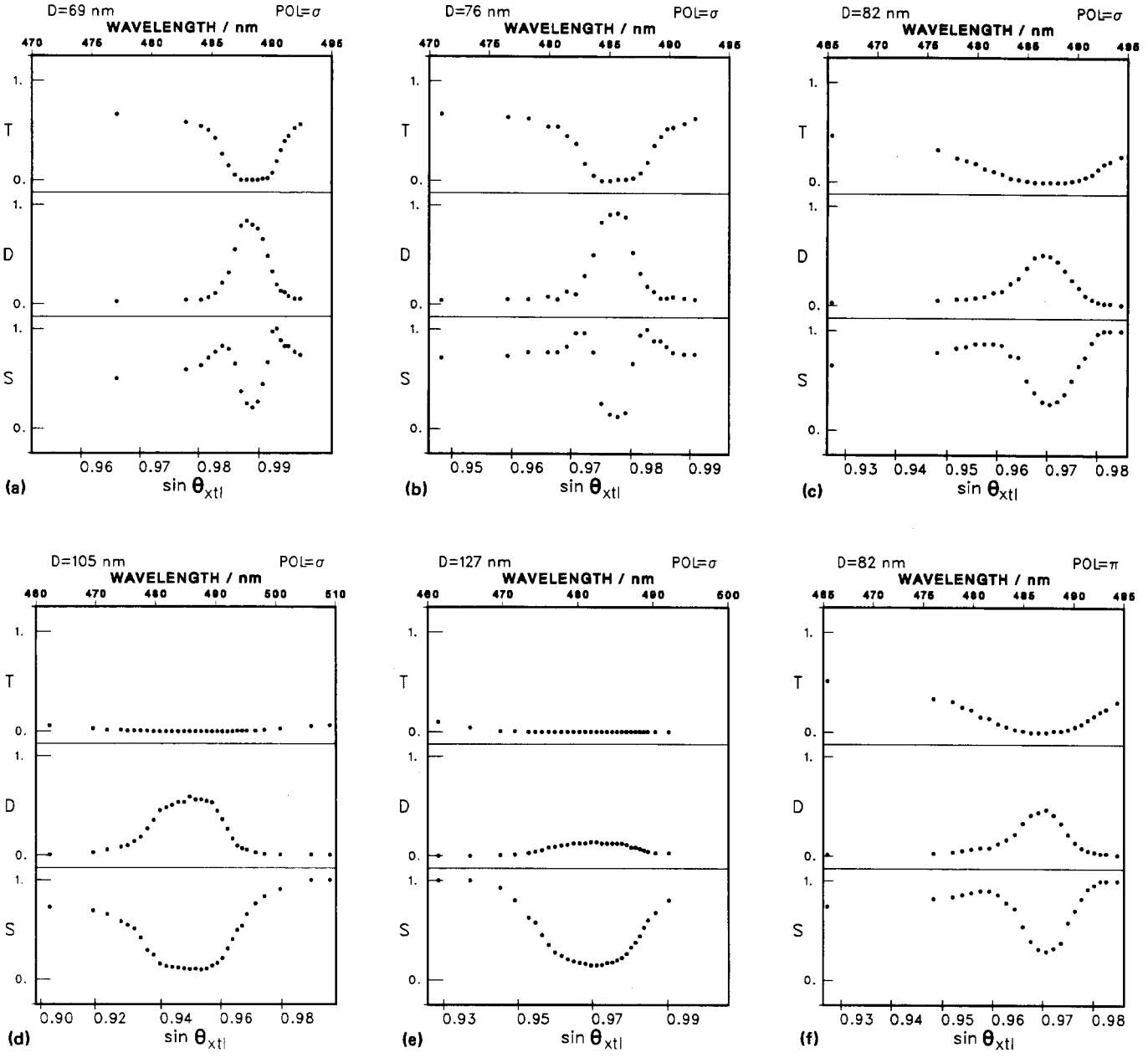

FIG. 5. Measured transmittance T, diffracted D, and diffusely scattered S intensities vs sin θ_{xtl} (bottom scale) and the wavelength in air (top scale) for the five crystals for σ-polarized incident beam, and for the 82 nm crystal for the π-polarized incident beam.

regions at the edge where twinning was not observed. The spatial profile of the incident beam was subtracted from each of these profiles in order to partially correct for the spot size of the beam. The figure clearly indicates that the diffuse scattering increases at the edge of the crystal. As discussed later, the increase in diffuse scattering results from an increase in the density of phonon states, dislocations, defects, etc., which destroy the rigid-lattice interference conditions. Ionic impurities, which migrate into the crystal at the edge, decrease the double-layer thickness to reduce the depth of the potential-energy minimum holding the spheres to their lattice sites. This results in a decrease in the restoring force for the spheres at the lattice site. In addition, defects such as dislocations must occur at the sample edge due to the sudden rough boundary of the sample spacer.

DISCUSSION

The diffraction of light by colloidal crystals is analogous to the diffraction of x rays by atomic crystals. The diffraction can be described as the result of interference between waves reflected by sets of parallel planes formed by the regular arrangement of the spheres on the crystal lattice sites. The condition for constructive interference is prescribed by Bragg's law, which forms the basis of the simple so-called kinematic diffraction theory. This theory, which assumes no

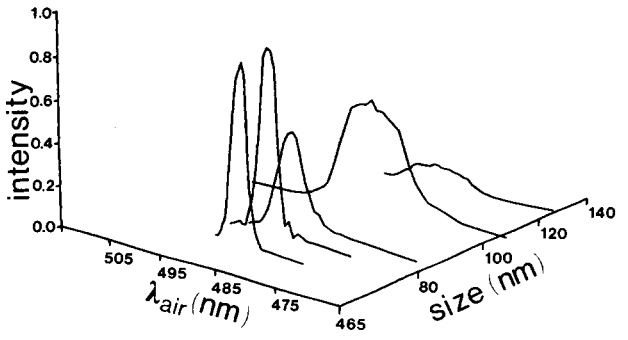

FIG. 6. Observed bandwidth and intensity dependence on sphere diameter for the five crystals studied. Wavelength scale was calculated using Bragg's law for the observed scattering angles (see text).

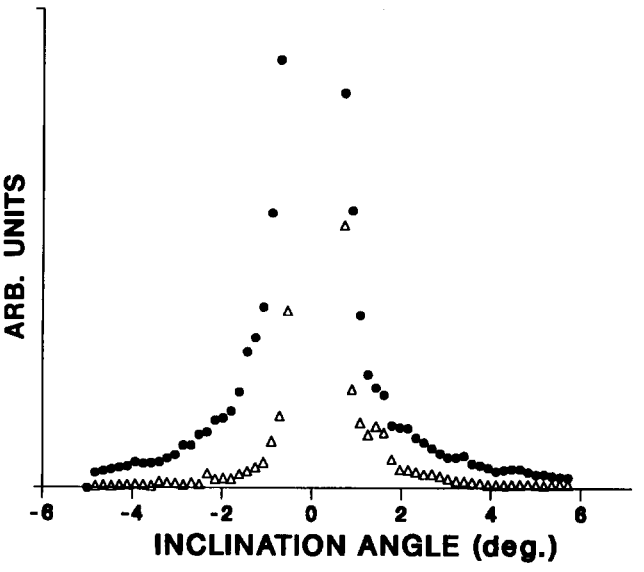

FIG. 7. Spatial profiles of two different regions of the 69 nm diameter sphere crystals. The solid circles are derived from an edge region while the triangles are derived from the well-ordered center region.

attenuation of the incident beam, semiquantitatively predicts the diffraction conditions. However, the description of the distribution of the intensity at and about the diffraction maximum requires a more detailed calculation, which takes into account multiple reflections and the effects of each reflection upon the phase of the waves. For such a description it becomes necessary to consider the coupling between the incident and diffracted waves in the crystal. The details of this dynamical diffraction theory have been extensively described in the literature.[41–43] In what follows we adopt the formalism of Zachariasen.[41]

The ordering of the polystyrene spheres produces a periodic variation of the polarizability per unit volume, $\alpha(\mathbf{r})$. This polarizability can thus be expanded in terms of the reciprocal-lattice vectors, $\mathbf{B}_H$:

$$4\pi\alpha(\mathbf{r}) = \psi(\mathbf{r}) = \sum_H \psi_H e^{-i2\pi\mathbf{B}_H\mathbf{r}}, \tag{4}$$

where

$$\psi_H = \frac{1}{V}\int \psi(\mathbf{r}) e^{i2\pi\mathbf{B}_H\mathbf{r}}\, dV. \tag{5}$$

V is the volume of the unit cell. We will use single and double primes to indicate the real and imaginary parts of the Fourier coefficients, ψ_H, respectively. The maximum diffracted intensity according to the dynamical diffraction theory occurs at an angle θ_m in the crystal given by

$$\theta^m_{xtl} = \theta^B_{xtl} + \frac{1-b}{2b\sin 2\theta^B_{xtl}}\psi_0', \tag{6}$$

where θ^B_{xtl} is the usual Bragg angle; b is the ratio of the direction cosines of the incident and diffracted waves relative to the surface normal, and for the geometry of our experiments b is negative and close to unity. Thus the real number ψ_0' scales the dynamical theory correction to the Bragg angle, i.e., the deviation of the center of the diffracted intensity profile from the direction predicted by Bragg's law. It is seen from the above equation, that the profile of the diffracted intensity is centered about an angle θ^m_{xtl} which is always smaller than the value predicted by Bragg's law. Similar considerations apply to the diffracted wavelengths. Here the theory predicts a red shift of the diffraction peaks, given by the following equation:

$$\lambda^m_{xtl} = \lambda^B_{xtl}\left(1 - \frac{1-b}{4b\sin^2\theta_{xtl}}\psi_0'\right), \tag{7}$$

where $\lambda^B_{xtl} = 2d\sin\theta^B_{xtl}$ and d is the spacing of the diffracting set of planes. In agreement with the calculations of Spry and Kosan[24] mentioned earlier, when the diffraction conditions are met, only a small number of colloidal sphere layers are necessary for essentially complete diffraction of the incident intensity. Therefore, we can use the dynamical diffraction theory formalism for thick crystals.[41] For a thick crystal the ratio of the diffracted power, P_H, to the incident power, P_0, for the set of planes H is given by

$$\frac{P_H}{P_0} = L - (L^2-1)^{1/2}, \tag{8}$$

where

$$L = |[(y^2-g^2-1)^2 + 4g^2y^2]^{1/2}| + y^2 + g^2, \tag{9}$$

and

$$y = \frac{(1-b)\psi_0' + b\alpha}{2\sqrt{|b|}K|\psi_H'|}. \tag{10}$$

The intensity profile of the diffracted beam is centered about the value $y = 0$. The attenuation of the incident beam by absorbance is measured by the quantity

$$g = \frac{(1-b)\psi_0''}{2\sqrt{|b|}K|\psi_H'|}. \tag{11}$$

K is a factor equal to 1 for the σ polarizatioon and $\cos 2\theta_{xtl}$ for the π polarization, and

$$\alpha = 2(\theta^B_{xtl} - \theta_{xtl})\sin 2\theta^B_{xtl}. \tag{12}$$

It is seen from Eq. (8) that for a nonabsorbing crystal (where $g = 0$) the intensity profile reaches a maximum value of 1, and is symmetric about $y = 0$ ($\theta_{xtl} = \theta^m_{xtl}$). As

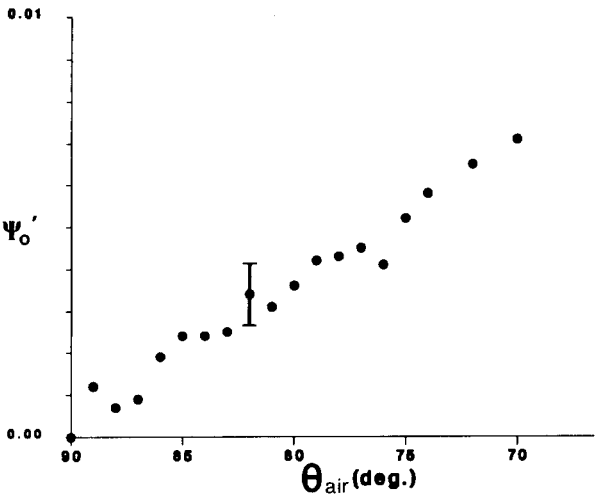

FIG. 8. Plot of the dynamical parameter ψ_0' as a function of the maximum diffraction angle for different wavelengths for an 82 nm sphere diameter crystal. The farther from normal incidence, the more significant the dynamical correction becomes.

pointed out earlier, the absorbance of polystyrene is negligible at the wavelengths of the experiment. Thus, any attenuation that is monitored by the parameter g is derived mainly from losses through various scattering mechanisms.

To determine the importance of the dynamical corrections to our measured colloidal diffraction angles and wavelengths, we measured λ^m_{air} as a function of θ^m_{air} and determined ψ_0' for different diffracted wavelengths by fitting the experimental data to Eqs. (6) and (7). We independently determined θ^B_{air} and the lattice parameter from Bragg's law, by measuring λ^B_{air} at $\theta_{air} = 90°$ and the crystal refractive index. The results for an 82 nm sphere diameter sample are plotted in Fig. 8, and show that the dynamical correction becomes increasingly significant as we depart from normal incidence. For example, at $\theta_{air} = 70°$ the difference $\theta^B_{xtl} - \theta^m_{xtl}$ is about 3°. Thus, measurements of the angles of maximum diffraction intensity for a given wavelength cannot be simply related to the crystal lattice spacing. The values of ψ_0' for the five samples used here are listed in Table II, along with the angles θ^m_{xtl} and θ^B_{xtl}. Table I lists and the interplanar distance d for each crystal. θ^m_{air} is measured directly from the experimental intensity profile.

TABLE II. Angles of maximum diffracted intensity, θ^m_{xtl}, for $\lambda = 488$ nm, measured from the intensity profiles, and angle calculated from Bragg's law, using the values from Table I. The quantity ψ_0' is evaluated from Eqs. (6) and (7).

D (nm)	θ^m_{xtl} (rad)	θ^B_{xtl} (rad)	ψ_0'
69	1.4267	1.4360	0.002 48
76	1.3613	1.3715	0.003 96
82	1.3283	1.3410	0.005 63
105	1.2610	1.2810	0.010 95
127	1.3376	1.3576	0.008 27

TABLE III. Measured bandwidths w (full width at half maximum) and best-fit values of the parameters g and ψ_H', and calculated values of w and ψ_H' using the structure factor from the Rayleigh–Gans approximation, using expressions of Spry and Kosan (Ref. 24).

	Experimental			Calculated	
D (nm)	g	w (nm)	ψ_H'	w (nm)	ψ_H'
69	0.115	3.0	0.0061	3.8	0.0066
76	0.063	3.5	0.0069	5.0	0.0084
82	0.356	5.7	0.0102	6.0	0.0102
105	0.304	13.3	0.0211	12.3	0.0201
127	1.205	12.5	0.0169	18.6	0.0315

We determined the parameters g and ψ_H' (Table III) by fitting the experimental intensity profiles to Eq. (8). The fits are shown in Fig. 9. The value of g determines the maximum diffracted intensity, while ψ_H' determines the bandwidth. The fits are very good for the smaller sphere diameters, but deteriorate noticeably for the 105 and 127 nm samples. Table III also displays the experimentally determined bandwidths and the calculated diffraction bandwidths in the thick crystal limit, calculated from Eq. (15) of Spry and Kosan.[24] In this case, the value of ψ_H' is obtained[4] from the scattering factor of a sphere in the Rayleigh–Gans approximation,[44,45] i.e.,

$$G(u) = (3/u^3)(\sin u - u \cos u), \tag{13}$$

where $u = (2\pi/\lambda)D \sin \theta^B_{xtl}$.

The Rayleigh–Gans approximation is expected to become less accurate as the sphere diameter D increases. It is seen that the calculated bandwidths are in good agreement with the experimental data, especially for the smaller diameters, in spite of the fact that the nonabsorbing crystal approximation[24] used is not justified for our crystals; the sum of the transmitted and diffracted intensities does not equal the incident intensity. In addition, the transmitted and diffracted peaks do not have the same bandwidth. Table III also lists the value of ψ_H' calculated from the G values [Eq. (13)] of the spheres in the unit cell. The calculated values are in very good agreement with the values derived from the best fit for all but the 127 nm sample. It is plausible that the observed deviation for the larger spheres reflects the inapplicability of the Rayleigh–Gans approximation for the 127 nm spheres, although additional errors introduced by static and phonon diffuse scattering cannot be excluded (see below).

While it appears that the dynamical diffraction theory shows reasonable agreement with the measured intensity profiles, a more detailed description would include the effects of random and collective motions of the particles, as is usually done in connection with x rays, and the effects of polydispersity in the size and surface charge of the spheres. In contrast to atomic crystals, the spheres making up the unit cells of the colloidal crystal are not perfectly monodisperse either in size or total charge, which must result in static irregularities in the colloidal crystal structure. The irregularities in the structure will alter the perfect lattice interfer-

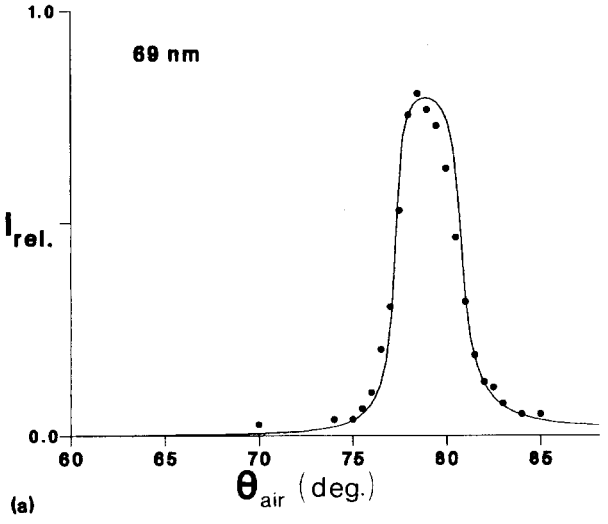

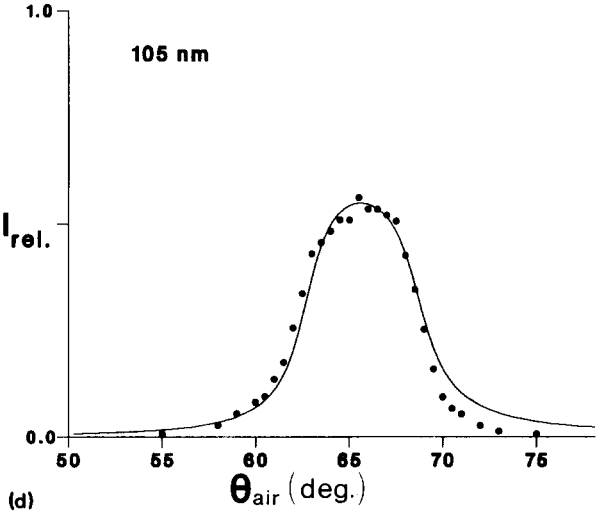

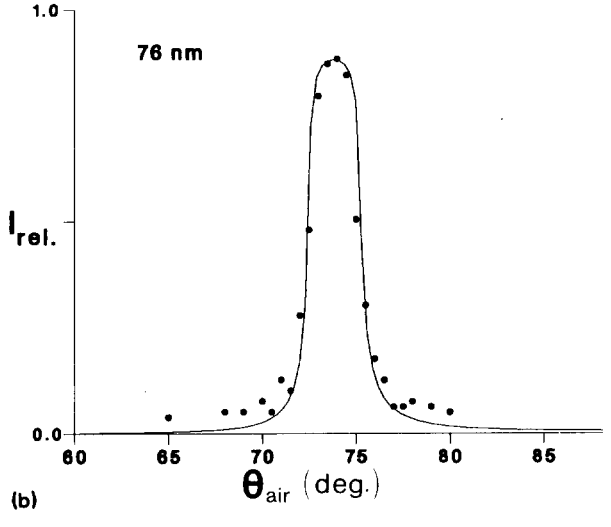

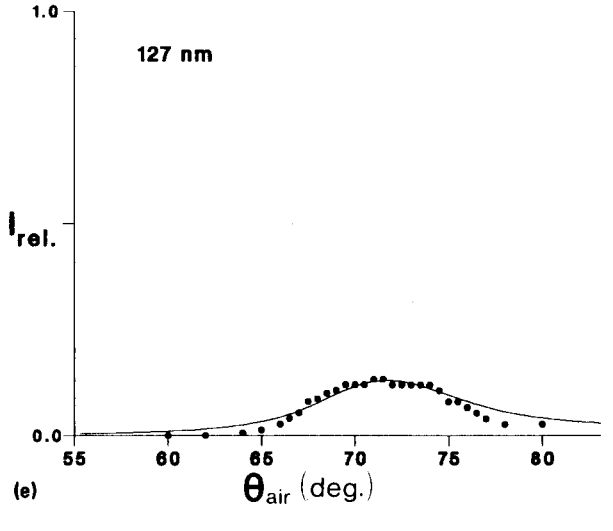

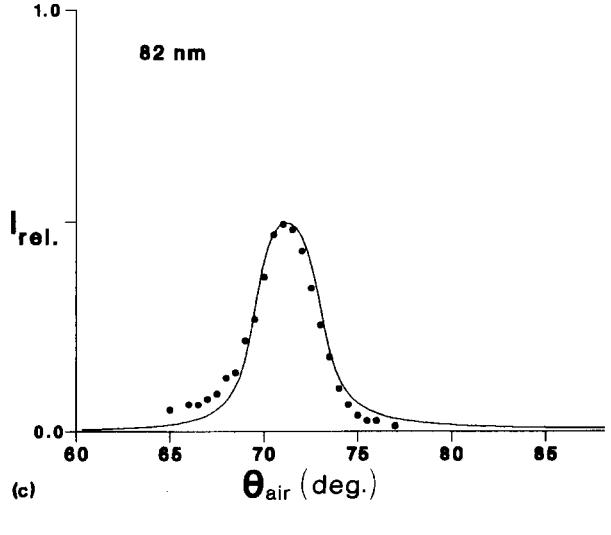

FIG. 9. Least-squares fits of the calculated dynamical diffraction profiles [Eq. (8)] to the experimental diffraction peaks. Both the calculated and experimental values are plotted vs θ_{air}. The best-fit values of the parameters g and ψ'_H are listed in Table III.

ence conditions, and thus broaden the diffraction bandwidths as well as scatter light in directions away from the rigid-lattice Bragg angle. Similar effects will also arise from the random thermal and collective motions of the spheres.

The diffusely scattered intensity I_s can be partitioned into two separate contributions, namely the incoherent I_n and the coherent I_c scattered intensities. Nonperiodic defects in the lattice structure give rise to the incoherent scattering. In general, such nonuniformities of the lattice structure do not have any directional preference, and the incoherent scattering is isotropic. The coherent contribution to the diffuse scattering arises from collective motions of the spheres associated with lattice phonons. Figure 10 shows the wave vectors describing these phonon modes about a reciprocal-lattice point for the 69 nm diameter sphere crystal. The Bragg condition can now be specified by $\mathbf{k}_D - \mathbf{k}_0 = \mathbf{B}_H + \mathbf{q}$, where $\mathbf{k}_D$ and $\mathbf{k}_0$ are the diffracted and incident wave vectors and $\mathbf{q}$ is the wave vector of a phonon mode. As shown in the figure, the phonon modes will result in a distribution of scattered wave vectors about the Bragg angle of the rigid lattice. This distribution depends on the directions represented by the vectors $\mathbf{q}$, and thus can result in an angular dependence. This angular distribution is the origin of the diffusely scattered intensity about the Bragg angle shown in Fig. 5. Thus, even at room temperature the phonon modes of the colloidal crystal contribute significantly to the diffuse scattering. The importance of the phonon modes in light scattering by colloidal crystal was demonstrated earlier by Hurd *et al.*,[38] who were also able to estimate the elastic constants of the collodial crystal. The elastic constants may also be estimated from careful measurements of the diffuse diffracted intensities.

The utility of these colloidal crystals as new optical devices derives from their diffraction efficiencies which effectively prevent all light at wavelengths meeting the Bragg condition from transmitting through the crystal. Indeed, the actual light transmission through our crystals is essentially zero for light at the Bragg condition. However, the actual transmitted intensity measured by a detector which monitors a large solid angle would significantly differ from zero due to the diffusely scattered light deriving from random defects and from lattice phonons. The contribution from the defects is angularly isotropic, and can be reduced by improving the size and charge monodispersity of the spheres as well as by minimizing the dislocation density. The diffuse scattering from phonons is anisotropic, reaching its largest values for angles of incidence displaced about the Bragg angle. We can minimize contrast degradation from diffuse scattering by ensuring that the acceptance angle of the detector is below the desired rejection bandwidth. As shown here, the bandwidth is controllable by selecting the appropriate sphere size.

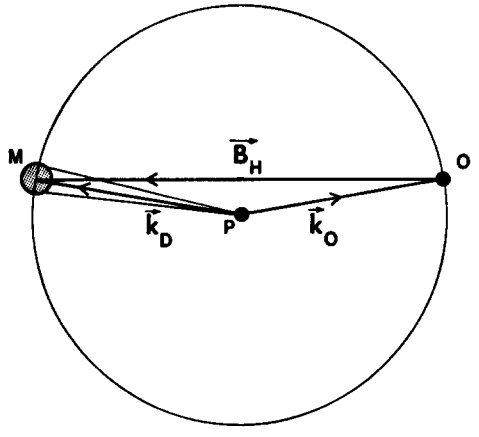

FIG. 10. Ewald reciprocal-space representation of the diffraction from the 69 nm diameter sphere crystal. The small shaded sphere about the reciprocal-lattice point M depicts the angular limits of diffracted light due to diffuse scattering.

SUMMARY

We demonstrate the fabrication of large crystals of polystyrene collodial arrays in bcc and fcc crystal structures. We show that the dynamical diffraction theory is required to account for the observed diffraction angles and the diffraction angular bandwidths. Our experimental results quantitatively agree with Spry and Kosan's previously presented simple theory for diffraction bandwidths and transmission from rigid periodic lattices, but clearly demonstrate that a more complex formalism is required to account for the diffraction intensities and the diffuse scattering phonomena. We observe a bcc to fcc phase transition which is induced by modestly increasing the sphere diameter while keeping the nearest sphere neighbor distances fixed. Finally, we discuss the impact of the diffuse scattering on the transmittance contrast available from these colloidal crystalline arrays. We are continuing our studies to complete our characterization and understanding of the phonon scattering.

ACKNOWLEDGMENTS

We gratefully acknowledge the help of Dr. Anastasia Morfesis and Perry L. Flaugh for taking some of the diffraction measurements. Sanford A. Asher is an Established Investigator of the American Heart Association.

[1]E. T. Samulski, and D. B. Dupré, J. Chim. Phys. **80**, 25 (1983).
[2]J. A. N. Zasadzinski and R. B. Meyer, Phys. Rev. Lett. **56**, 636 (1986).
[3]W. Luck, M. Klier, and H. Wesslau, Ber. Bunsenges. Phys. Chem. **67**, 75 (1963).
[4]P. A. Hilter and I. M. Krieger, J. Phys. Chem. **73**, 2386 (1969).
[5]P. A. Hiltner, Y. S. Papir, and I. M. Krieger, J. Phys. Chem. **75**, 1881 (1971).
[6]R. H. Ottewill, Langmuir **5**, 4 (1989).
[7]C. J. Barnes, D. Y. C. Chan, D. H. Everett, and D. E. Yates, J. Chem. Soc. Faraday Trans. II **74**, 136 (1978).
[8]P. Pieranski, Contemp. Phys. **24**, 25 (1983).
[9]D. Hone, S. Alexander, P. M Chaikin, and P. Pincus, J. Chem. Phys. **79**, 1474 (1983).
[10]S. Alexander, P. M. Chaikin, P. Grant, G. J. Morales, P. Pincus, and D. Hone, J. Chem. Phys. **80**, 5776 (1984).
[11]D. J. W. Aastuen, N. A. Clark, L. K. Cotter, and B. J. Ackerson, Phys. Rev. Lett. **57**, 1733 (1986).
[12]S. Hachisu and S. Yoshimura, *Physics of Complex and Supermolecular Fluids*, edited by N. A. Clark and S. Safran, Exxon Monographs (Wiley-Interscience, New York, 1987), p. 321.
[13]T. Okubo, J. Chem. Soc. Faraday Trans. 1 **82**, 3163 (1986); **84**, 1949

(1988); Acc. Chem. Res. **21**, 281 (1988).
[14]H. O. Moser, O. Fromheim, F. Herrmann, and H. Versmold, J. Phys. Chem. **92**, 6723 (1988).
[15]P. A. Forsyth, S. Marcelja, D. J. Mitchell, and B. W. Ninham, Adv. Colloid Interface Sci. **9**, 37 (1978).
[16]J. Th. G. Overbeek, Powder Technol. **37**, 195 (1984).
[17]M. E. Woods, J. S. Dodge, I. M. Krieger, and P. E. Pierce, J. Paint Technol. **40**, 541 (1968).
[18]J. S. Dodge, M. E. Woods, and I. M. Krieger, J. Paint Technol. **42**, 71 (1970).
[19]Y. S. Papir, M. E. Woods, and I. M. Krieger, J. Paint Technol. **42**, 571 (1970).
[20]R. Williams and R. S. Crandall, Phys. Lett. **42A**, 225 (1974).
[21]J. W. Goodwin, R. H. Ottewill, and A. Parentich, J. Phys. Chem. **84**, 1580 (1980).
[22]P. L. Flaugh, S. E. O'Donnell, and S. A. Asher, Appl. Spectrosc. **38**, 847 (1984).
[23]S. A. Asher, P. L. Flaugh, and G. Washinger, Spectroscopy **1**, 26 (1986).
[24]R. J. Spry and D. J. Kosan, Appl. Spectrosc. **40**, 782 (1986).
[25]S. Hagopian, J. Conners, and S. A. Asher (to be published).
[26]J. W. Vanderhoff and H. J. Van den Hul, J. Colloid Interface Sci. **28**, 336 (1968).
[27]H. J. Van den Hul and J. W. Vanderhoff, J. Electroanal. Chem. **37**, 161 (1972).
[28]J. W. Vanderhoff and H. J. Van den Hul, J. Macromol. Sci. Chem. **7**, 677 (1973).
[29]S. A. Asher, U. S. Patents Nos. 4,627,689 and 4,632,517.
[30]R. J. Carlson and S. A. Asher, Appl. Spectrosc. **38**, 297 (1984).
[31]J. B. Bateman, E. J. Weneck, and D. C. Eshler, J. Colloid. Sci. **14**, 308 (1959).
[32]N. A. Clark, A. J. Hurd, and B. J. Ackerson, Nature (London) **281**, 57 (1979).
[33]P. Pieranski, E. Dubois-Violette, F. Rothen, and L. Strzelecki, J. Phys. (Paris) **42**, 53 (1981).
[34]D. H. Van Winkle and C. A. Murray, Phys. Rev. A **34**, 562 (1986); C. A. Murray and D. H. Van Winkle, Phys. Rev. Lett. **58**, 1200 (1987).
[35]S. Hachisu, Y. Kobayashi, and A. Kose, J. Colloid Interface Sci. **42**, 342 (1973).
[36]K. Takano and S. Hachisu, J. Chem. Phys. **67**, 2604 (1977).
[37]S. Mitaku, T. Ohtsuki, K. Enari, A. Kishimoto, and K. Okano, Jpn. J. Appl. Phys. **17**, 305 (1978).
[38]A. J. Hurd, N. A. Clark, R. C. Mockler, and W. J. O'Sullivan, Phys. Rev. A **26**, 2869 (1982).
[39]S. L. Brenner, J. Phys. Chem. **80**, 1473 (1976).
[40]I. Sogami and N. Ise, J. Chem. Phys. **81**, 6320 (1984).
[41]W. H. Zachariasen, *Theory of X-Ray Diffraction in Crystals* (Wiley, New York, 1945), Chap. 3.
[42]B. W. Batterman and H. Cole, Rev. Mod. Phys. **36**, 681 (1964).
[43]Z. Pinsker, *Dynamical Scattering of X-Rays in Crystals* (Springer-Verlag, Berlin, 1978), Chaps. 7 and 8.
[44]H. C. van de Hulst, *Light Scattering by Small Particles* (Dover, New York, 1981), Chap. 7.
[45]C. F. Bohren and D. R. Huffman, *Absorption and Scattering of Light by Small Particles* (Wiley, New York, 1983), Chap. 6.